

# DustNet: A Wireless Network of Ultrasonic Neural Implants

Jade Pinkenburg<sup>\*1</sup>, *Graduate Student Member, IEEE*, Changuk Lee<sup>\*1</sup>, *Member, IEEE*, Mohammad Meraj Ghanbari<sup>\*1</sup>, *Member, IEEE*, Cem Yalcin<sup>1</sup>, *Member, IEEE*, Miguel Montalban<sup>1</sup>, and Rikky Muller<sup>1,2</sup>, *Senior Member, IEEE*

**Abstract**—Spatially distributed peripheral nerve recordings can be used to reconstruct motor intention and improve natural control of prosthetics in patients with limb deficiencies. However, many existing clinical solutions rely on percutaneous wires to access peripheral nerves; these sites are prone to infection and electrode degradation, preventing chronic use. To enable long-term recording of deeply-seated peripheral nerves, this paper presents DustNet: a network of ultrasonically-powered neural recording implants capable of supporting up to 8 simultaneously-recording nodes over a single ultrasound link. To enable high-throughput multi-implant communication, DustNet implements a time-division multiple-access (TDMA) protocol with up to 16-level amplitude modulation of the ultrasound backscatter that achieves up to 4x higher data rates than traditional on-off keying methods. Each neural implant consists of a  $0.7 \times 0.7 \times 0.7 \text{ mm}^3$  piezoceramic transducer, a  $10 \text{ nF}$  off-chip capacitor, and an IC mounted on a flexible PCB. The implant IC was fabricated in a 28nm CMOS process and occupies an area of  $0.43 \text{ mm}^2$ . System functionality was verified within FDA power limits at 90mm depth, achieving a maximum data rate of  $400 \text{ kb/s}$  at 2 MHz ultrasound carrier frequency, with each implant transmitting uplink data at  $50 \text{ kb/s}$  and dissipating just  $7 \mu\text{W}$  of power.

**Index Terms**—Amplitude-shift keying, echo modulation, implantable biomedical device, neural recording, piezoelectric, TDMA, ultrasound

## I. INTRODUCTION

PERIPHERAL nerves are responsible for carrying motor and sensory signals throughout the body; developing implantable devices to record activity from these nerves has myriad applications in basic neuroscience, disease diagnosis, and therapeutic treatments [1]. For example, recordings of efferent motor nerve signals from functional nerve endings retained by patients with limb deficiencies can be used to decode motion intention. Recent studies have demonstrated that real-time activity data recorded from these nerves can be used to significantly improve the performance of prosthetic limbs and give patients more intuitive and reliable control over these devices [2]. However, existing clinical efforts have primarily relied on percutaneous wires to connect external circuitry with implanted neural electrodes. These sites tend

This work was supported in part by the National Science Foundation (NSF) Graduate Research Fellowship Program under Grant No. DGE 2146752 and in part by the Weill Neurohub Fellowship.

C. Lee, J. Pinkenburg, M.M. Ghanbari, C. Yalcin, and M. Montalban are with the Department of Electrical Engineering and Computer Sciences, University of California at Berkeley, Berkeley, CA, 94720 USA.

R. Muller is with the Department of Electrical Engineering and Computer Sciences, University of California at Berkeley, Berkeley, CA, 94720 USA and also with Weill Neurohub, Berkeley, CA, 94720 USA.

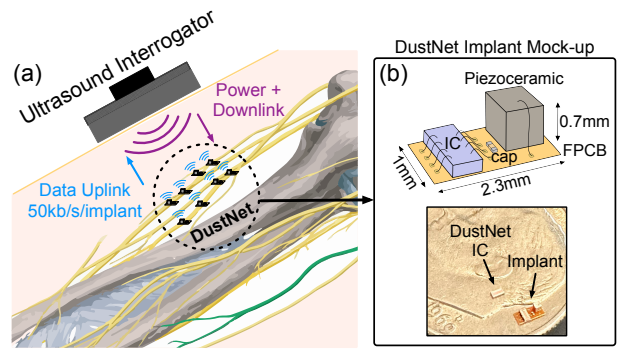


Fig. 1. (a) Conceptual diagram of the proposed DustNet wireless neural recording platform with 8 implanted sensor nodes. (b) Implant mock-up diagram and assembly with a US dime for reference.

to be very susceptible to infection. External forces on the wires can also cause signal quality to degrade over time by shifting the electrode placement. As a result, the percutaneous electrodes must be explanted after several weeks, preventing long-term use [3].

In contrast, miniaturized neural recording implants with wireless power transfer and data transmission enable chronic recording of peripheral nerve activity with minimal invasiveness to the patient. Because several distinct nerves coordinate limb movement, a spatially-distributed network of simultaneously recording implants is required to ensure dexterous control of limb prosthetics. Previous works have demonstrated networks of multiple neural recording implants using radiofrequency (RF), near-infrared (NIR), magnetoelectric (ME), or ultrasound (US) links [4]–[8]. Although RF carrier frequencies enable high overall data rates, the high attenuation coefficient of RF energy in tissue severely limits the depth of these implants [4], preventing recording from deeply-seated peripheral motor nerves; NIR similarly suffers from significant attenuation in tissue [5]. Conversely, magnetoelectric links penetrate deep into tissue with low loss, but suffer from limited per-implant data rates (less than  $10 \text{ kb/s/implant}$ ) [6]. In contrast, US links enable low-loss communication in the body while offering sufficient channel bandwidth to support transmission of continuous neural activity data at depth [7], [8]. Because the transducer size often dominates the overall wireless implant volume, US links also enable mm-scale implant miniaturization due to the sub-mm wavelength of US in the body at frequencies of interest [9]. The safety limit for transmitted US power in the body is also significantly higher than that for RF

energy, resulting in higher received power at the implant and further enabling transducer miniaturization. However, increasing tissue absorption at higher frequencies limits US carrier frequencies to the low-MHz range in the human body.

To accurately record neural data for use in spike sorting or local field potential (LFP) reconstruction, an implant data rate of at least 50 kb/s is required [10]. Prior clinical studies have demonstrated that recording from 8 distinct nerves is sufficient to achieve near-natural control over limb prosthetics [2]. Thus, a total system data rate of at least 400 kb/s is required to ensure continuous and intuitive prosthetic control. To enable recording from deeply-seated motor nerves (e.g., sciatic nerve for leg prosthetics), the implants must also be able to operate at depths of over 50mm. Although US links have been demonstrated to power implants at this depth in tissue, the low US carrier frequency necessitates a spectrally-efficient communication scheme to achieve the required system data rate. To address these challenges, we present DustNet: a network of wireless, ultrasonically-powered neural implants capable of supporting up to 8 simultaneously recording implants using a single US link for power transfer and bidirectional data communication. DustNet implements a custom time-division multiple-access (TDMA) protocol to communicate with multiple implants while minimizing inter-implant interference. To achieve a high data rate despite the low carrier frequency of ultrasound in the human body, we introduce a spectrally-efficient 16-level amplitude shift keying (ASK) modulation scheme to encode multiple bits per symbol in the US backscatter. Using these techniques, DustNet achieves an overall data rate of 400 kb/s at 2 MHz US carrier frequency, with a per-implant data rate of 50 kb/s. Each implant occupies a volume smaller than 0.5 mm<sup>3</sup> and consumes 7  $\mu$ W. System operation is verified at 90mm depth in a tissue phantom and the bit-error rate (BER) of the communication protocol is measured to be at most 1.89E-5.

This paper is an extension of [11], and offers an extended discussion of the TDMA communication protocol, analysis of the multi-level ASK backscatter scheme, an updated circuit implementation including an analog front-end for recording neural signals, and presents additional measurement results. Section II discusses the communication protocol, Section III explains the chip implementation, and section IV reports the measurement results. Section V presents a comparison against state-of-the-art neural implants and summarizes this work.

## II. COMMUNICATION PROTOCOL

### A. System Overview

Fig. 1 illustrates the proposed wireless neural recording system. DustNet consists of an unfocused ultrasound transducer external to the body and up to 8 free-floating neural recording devices implanted on peripheral nerves. The external transducer is placed in contact with the skin and transmits US pulses through tissue; the implants each harvest power using a miniaturized piezoceramic transducer (piezo) to convert the mechanical US wave into an electrical AC signal that is rectified to DC power by the implant IC and stored on an off-chip capacitor. To transmit data, the implants utilize

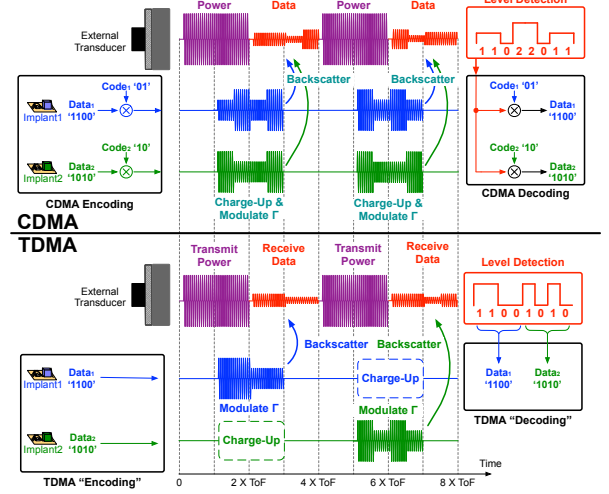


Fig. 2. Timing diagram for pulse-echo communication using CDMA and TDMA protocols. During uplink, the maximum achievable data rate for both protocols is identical, but TDMA is more robust to inter-implant mismatch and allows implants to charge without sacrificing channel bandwidth.

a power-efficient pulse-echo communication scheme in which the implant encodes data in the backscattered acoustic wave.

### B. Multiple-Access Ultrasound Communication

Previous work has demonstrated full-duplex ultrasound communication with continuous power transfer by using one piezo for downlink power and data while actively driving a second piezo for uplink communication [12]. However, the large power consumption demanded by the active drive circuitry limits the implant depth and the second piezo significantly increases the implant volume. To minimize implant size and power consumption, DustNet employs a single-piezo, pulse-echo communications scheme that eliminates the need for active drive, as demonstrated in [7], [13]. To transmit data, each implant modulates the acoustic reflection coefficient ( $\Gamma$ ) of its piezo to encode data on the backscattered acoustic wave. Simultaneous bidirectional transmission is avoided due to the high dynamic range required to operate the transducer in both RX and TX mode; TX mode requires high-voltage (50V<sub>pp</sub>), and the reflected waves generate received signal voltages of just a few mV<sub>pp</sub> in RX mode.

To enable communication with multiple implants, previous works have employed cellular techniques such as TDMA [14], code-division multiple access (CDMA) [7], [8], and frequency-division multiple access (FDMA) [14] protocols for data transmission over an ultrasound link, all of which are compatible with a pulse-echo communication scheme. Because the implant piezos have a narrow bandwidth, FDMA is difficult to implement for large systems since it necessitates that the implant piezos are of precise, varying sizes to generate different resonant frequencies; this significantly increases overall system complexity, making CDMA and TDMA protocols much more practical choices. Assuming perfect use of the available channel bandwidth, the channel capacity of CDMA and TDMA communication links are

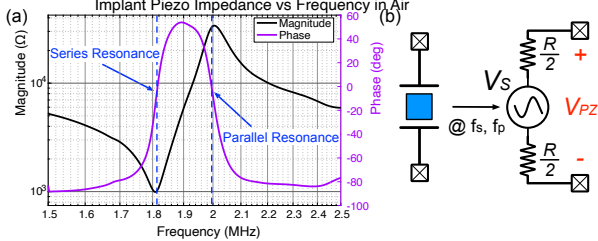


Fig. 3. (a) Typical implant piezo impedance as a function of frequency. At resonance ( $f_s$  and  $f_p$ ), the piezo impedance is purely resistive. (b) Piezo electrical model at resonance. The resistance at the series resonance is significantly lower than the resistance at the parallel resonance.

identical for a fixed carrier frequency, as shown in Fig. 2. However, CDMA is particularly sensitive to variations in implant depth and mismatches in the signal power transmitted by each implant. For example, [8] introduces an ISI-tolerant US CDMA decoder that supports high total data rates, but required a complex machine learning receiver architecture to correct for path differences and implant mismatch. In contrast, TDMA is robust to implant mismatch and inter-implant interference caused by depth variations while still enabling high data rates [14]. Furthermore, a TDMA protocol enables implants to store charge while not in control of the channel.

To receive data from multiple implants, DustNet employs a custom pulse-echo TDMA protocol in which channel control cycles sequentially between implants. In this protocol, the external transducer continuously transmits power pulses to the implants and only one implant backscatters data on each pulse. The remaining implants harvest power from the US pulse and charge their storage capacitors. The uplink order is assigned during implant configuration, and the implants count the incoming US pulses to keep track of channel control. The external transducer and implants must be aligned such that each DustNet node receives sufficient US power and the backscattered wave is incident on the transducer surface.

### C. Multi-Level ASK Modulation

Modulating the acoustic reflection coefficient by adjusting the piezo termination impedance  $Z_E$  encodes data on the amplitude of the backscattered wave. However, the nonlinear relationship between  $\Gamma$  and  $Z_E$  caused significant distortion in previously developed analog backscatter modulators [13], [15]. To mitigate the effects of signal distortion and maximize modulation depth, previous works have implemented binary ASK backscatter modulation schemes to transmit uplink data [16], [17]. This also minimizes system complexity by using a simple switch as the termination impedance. At the series resonance, opening the switch forces  $\Gamma=1$  and closing the switch forces  $\Gamma=0$ ; the opposite is true at the parallel resonance. A 2-level ASK modulation scheme is also significantly more robust to carrier and electronic noise, enabling low BER. However, the overall system data rate is constrained by the time required to transmit each bit; the large spacing between echo voltages also reduces the spectral efficiency of the modulation scheme. In contrast, the data rate

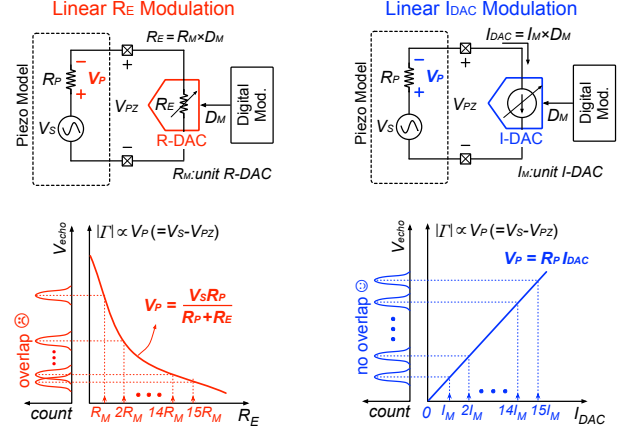


Fig. 4. Multi-level ASK modulation: (a) Using a linear R-DAC and (b) using a linear I-DAC.

and BER of analog modulation schemes are primarily limited by carrier noise [7]. To combine the advantages of binary ASK modulation and analog amplitude modulation, a quasi-digital multi-level ASK modulation scheme ensures robustness to noise while maintaining a high data rate.

To implement the linear backscatter modulator required for multi-level backscatter amplitude modulation, accurate modeling of the implant piezo is required. Recent work has demonstrated that at resonance,  $\Gamma$  is dependent on the electrical impedance across the piezo terminals and the internal impedance of the piezo [9]. A typical impedance profile of the implant piezo as a function of frequency is shown in Fig. 3(a), and it exhibits two resonant frequencies: a series resonant frequency ( $f_s$ ) at 1.82 MHz and a parallel resonant frequency ( $f_p$ ) at 2.00 MHz. The piezo impedance is much higher at the parallel resonant frequency than at the series resonant frequency. At resonance, the impedance of the piezo is purely resistive, and the transducer can be modeled as a Thevenin equivalent circuit without reactive components, as shown in Fig. 3(b). Equations (1) and (2) demonstrate how  $\Gamma$  is determined for the series and parallel resonant frequencies, where  $Z_{Th}$  is the Thevenin equivalent resistance at resonance and  $Z_E$  is the termination impedance across the piezo terminals.

$$\Gamma_p \propto \frac{Z_{Th,s}}{Z_E + Z_{Th,s}} \quad \Gamma_s \propto \frac{Z_E}{Z_E + Z_{Th,p}} \quad (1, 2)$$

$$\Gamma_p \propto V_S - V_{PZ} \quad \Gamma_s \propto V_{PZ} \quad (3, 4)$$

Multi-level ASK modulation can be easily implemented using a resistive digital-to-analog converter (R-DAC) as the termination impedance. However, linearly spaced R-DAC resistances would result in nonlinear spacing of the received backscatter amplitude and increase the BER due to carrier and electronic noise, as shown in Fig. 4(a). Furthermore, if nonlinearly spaced resistances were used to generate linear echo levels, variations in R-DAC levels would be amplified by the nonlinear relationship between  $\Gamma$  and  $Z_E$ . To create linearly spaced backscatter levels that minimize the system BER, we can instead modulate the voltage across the piezo terminals. Rewriting Equations (1) and (2) demonstrates that  $\Gamma$  is linear

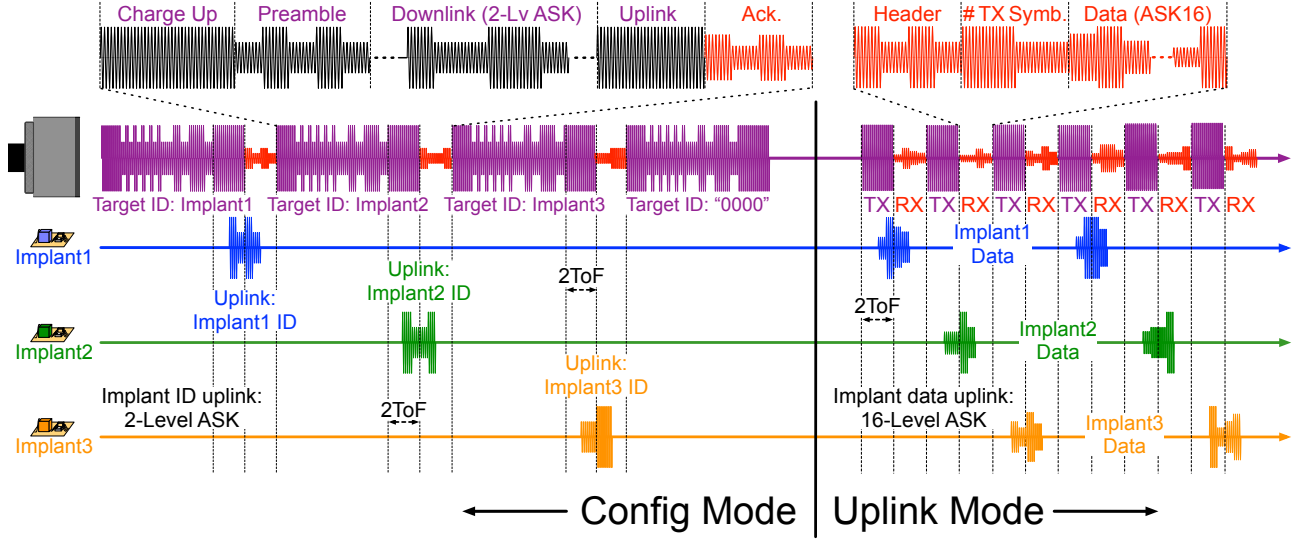


Fig. 5. Complete timing diagram of the DustNet communication protocol. In Config Mode, the external transducer transmits pulses that encode link parameters and a target implant ID. Implants matching the target ID backscatter the ID to acknowledge successful configuration. A transmitted target ID of 0 signals implants to transition to Uplink Mode, which implements the TDMA protocol for data transmission.

TABLE I  
PROGRAMMABLE UPLINK PARAMETERS

Parameter	Range	Description
I-DAC Unit Current	4 - 40 $\mu$ A	Account for piezo resistance variations
Number of Uplink Samples per Packet	1 - 16	Enables varying implant depths
ASK Levels	2, 4, 8, 16	Adjust data rate for noisy channels
Total Number of Implants	1 - 8	Communicate with multiple implants
Uplink Index	1 - 8	Sets order of channel control in Uplink Mode
LFSR Enable	1 or 0	Enable LFSR for BER characterization
Number of Cycles per Symbol	4, 6, 8, 10, 12, 14, 16	Adjust symbol rate for piezo settling time
ADC Slice Selection	0-7; 1-9; 2-10; 3-11	Sets ADC range

in the piezo voltage  $V_{PZ}$  (Equations (3-4)). Because the piezo impedance is purely resistive at resonance,  $\Gamma$  is linearly related to the current across the piezo terminals. Therefore, linearly spaced backscatter levels can be easily realized using a current DAC (I-DAC), as shown in Fig. 4(b). Because the effective resistance of the piezo is higher at parallel resonance, the carrier frequency of the transmitted ultrasound frequency is chosen to match  $f_p$  of the implant piezo to achieve larger modulation of  $\Gamma$ . In this scheme, the number of ASK levels is limited by the carrier, I-DAC, and channel noise.

#### D. Communication Protocol Implementation

To enable high-speed communication and link configuration, DustNet implements two modes of operation: Config Mode and Uplink Mode. Upon powering up, all implants first enter Config Mode. In Config Mode, the external transducer encodes data in the amplitude of the transmitted wave to program link parameters for each implant.

As shown in Fig. 5, Config Mode pulses consist of four sections: (1) charge-up, (2) preamble, (3) downlink data, and (4) uplink. The charge-up section is transmitted at maximum amplitude and is used by each implant to charge its storage capacitor. During the preamble, the amplitude of the incoming US wave is modulated by the external interrogator using 2-level ASK. The pattern "10" is repeated 32 times so that the implants can estimate the downlink symbol width. The number of ultrasound cycles transmitted per symbol is configurable to ensure proper implant configuration in the presence of transducer or piezo variations. Symbol width is estimated by averaging the number of ultrasound cycles transmitted in each "1" and "0". At the end of the preamble, a "11001100" header pattern is transmitted to indicate the end of the preamble. The subsequent downlink data section consists of 48 Manchester encoded link configuration bits. The implants use the previously measured symbol width to sample each symbol at its midpoint and compare the sampled voltage to the average envelope voltage to extract the digital symbol; Manchester encoding ensures that the average envelope voltage remains constant. To indicate which implant is being configured, the first 8 bits are reserved for a target implant ID. Each implant has a hard-coded ID assigned using pads on the DustNet IC; if the implant ID matches the transmitted target ID, the implant stores the new link parameters. A list of configuration parameters programmed in Config Mode is enumerated in Table I. Once all the configuration bits are sent, the last portion of the Config Mode pulse is reserved for implant uplink. If the target ID matches the hard-coded implant ID, the implant will backscatter a "0101" header followed by its own ID to acknowledge successful configuration. This also enables the external transducer to discover how many implants are in the system by sweeping all available implant IDs and observing which IDs receive a response.

Once all implants have been configured, the DustNet system moves to Uplink Mode. The external transducer indicates the

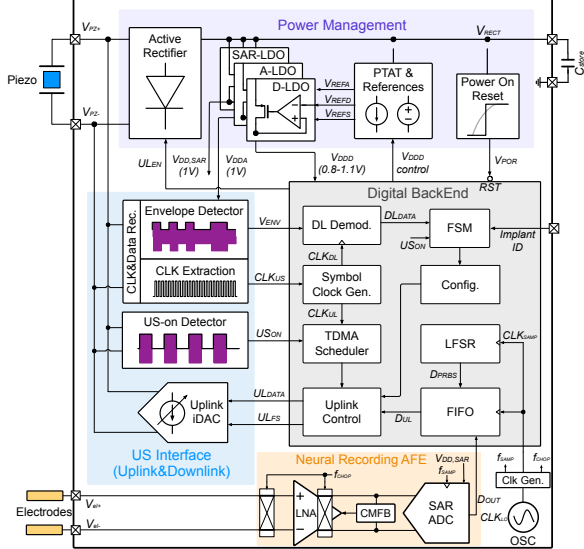


Fig. 6. DustNet IC block diagram, including power management blocks, the neural recording AFE, a digital backend, and the ultrasound interface. The electrodes, implant piezo, storage capacitor, and hard-wired ID fuses are externally connected to pads on the IC.

start of Uplink Mode by transmitting a reserved chip ID (“00000000”) in the final Config Mode pulse; all subsequent pulses are Uplink Mode pulses, which consist of a short charge-up segment, a header segment, and a data segment. As in Config Mode, implants use the charge-up segment to charge their storage capacitor. During the header segment, implants use the uplink modulator to transmit a “1010” header and the number of data samples transmitted in the Uplink Mode pulse on the amplitude of the backscattered wave using 2-level ASK modulation. The header is followed by data encoded using  $2^M$ -level ASK modulation, where M is a configurable integer from 1-4. The number of US cycles transmitted per symbol is programmable in Config Mode. As shown in the Uplink Mode timing diagram in Fig. 5, only one implant backscatters data during each Uplink Mode pulse; the order in which implants transmit data is programmed in Config Mode.

### III. CIRCUIT IMPLEMENTATION

Fig. 6 shows the block diagram of the DustNet IC. The IC has 5 main blocks: (1) power management, including an active rectifier and low-dropout regulators (LDOs); (2) an ultrasound interface with downlink data processing and a linear, multi-level ASK uplink modulator; (3) a low-noise neural recording analog front-end (AFE); (4) on-chip clock generators; and (5) a digital backend to manage the communication protocol. During operation, the implants continuously record neural data using the AFE and store it on an on-chip first-in first-out (FIFO) memory. Once powered on by the first incoming US pulse, the implants do not turn off; pulses are structured such that the implants can store enough energy to stay powered during inter-pulse gaps.

### A. Power Management and Integrated Uplink Modulator

The active rectifier converts the AC voltage transduced by the piezo into a DC voltage ( $V_{rect}$ ) that is stored on a

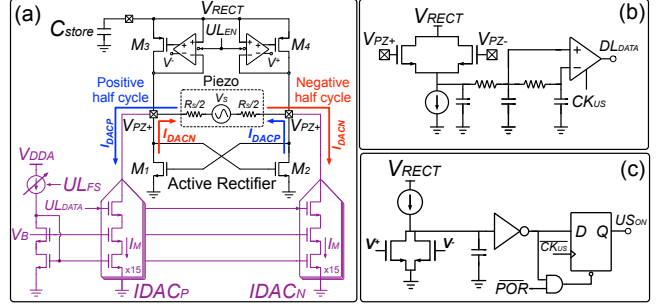


Fig. 7. (a) Active rectifier with integrated linear 16-level uplink modulator. (b) Envelope detector circuitry to process downlink data. (c) Ultrasound-on-detector circuitry to detect the start of TX pulses.

10 nF capacitor ( $C_{store}$ ).  $V_{rect}$  varies with the amplitude of the received US wave and drops during the gap between US pulses, but always exceeds 1.2V after start-up to ensure stable system functionality. LDOs regulate the variable  $V_{rect}$  to create stable voltages for the analog ( $V_{DD,A}$ , 1V) and digital ( $V_{DD,D}$ , 0.8V) supply domains, as well as a separate 1V supply for the SAR ADC. A supply-independent, proportional-to-absolute-temperature (PTAT) reference circuit provides voltage references ( $V_{REF,A}$ ,  $V_{REF,D}$ ) for the LDO blocks. Once the LDO outputs are settled, a power on reset (POR) block raises a flag ( $V_{POR}$ ) to activate the digital backend and begin data sampling.

The uplink modulator consists of two 16-level linear I-DACs ( $I_{DACP}$  and  $I_{DACN}$ ) integrated into the active rectifier topology, as shown in Fig. 7. When the rectifier is actively harvesting power from the piezo, the I-DACs are disabled and pass transistors  $M_3$  and  $M_4$  are toggled such that the positively charged piezo terminal is connected to  $C_{store}$  if  $|V_{PZ}| > V_{RECT}$ . During data uplink, the digital backend turns off  $M_3$  and  $M_4$  to protect the stored charge on  $C_{store}$  from the large I-DAC currents. The I-DACs consist of 15 identical, switchable current sources that can each pull a current  $I_M$  through the piezo. The number of enabled sources corresponds to the amplitude of the backscattered symbol. Using an adjustable current mirror sourced from a PTAT reference,  $I_M$  is configurable from  $4\mu\text{A}$  to  $40\mu\text{A}$  to account for variations in the piezo impedance across implants. The current mirror ratio is large to ensure low quiescent power consumption.  $I_{DACP}$  conducts current during the positive half-cycle of the incoming US wave, and  $I_{DACN}$  conducts current during the negative half-cycle to preserve the sign of  $\Gamma$  modulation.

## *B. Ultrasound Interface & Digital Backend*

The communication protocol and data sampling are managed by the digital backend. After V<sub>POR</sub> is raised during start-up, the digital backend begins to write data from the ADC (D<sub>OUT</sub>) or LFSR (D<sub>PRBS</sub>) into the FIFO memory. The 6.25 kHz CLK<sub>samp</sub> serves as the write enable for the FIFO memory and advances the LFSR code.

In Config Mode, an envelope detector circuit processes the symbols transmitted by the external interrogator ( $V_{ENV}$ ), which are demodulated and processed by a finite-state machine (FSM). To identify the downlink symbols ( $DL_{DATA}$ ), the

envelope detector compares the instantaneous US envelope voltage with the average envelope voltage using two low-pass filters with different corner frequencies, as shown in Fig. 7(b). The FSM processes the downlink data and updates the link parameters stored in configuration registers if the transmitted target ID matches the externally hard-coded implant ID set using pads on the IC.

During Uplink Mode, 8 or 9 bits of the FIFO output ( $D_{UL}$ ) are selected and assembled into M-bit transmission packets ( $UL_{DATA}$ ) by the uplink control module for  $2^M$ -level ASK communication; 8 bits are selected for 2,4, and 16-level ASK modulation, while 9 bits are selected for 8-level ASK modulation to ensure an integer number of symbols per data sample. The bits selected from the 12-bit ADC output are customizable in Config Mode; this enables a configurable ADC range to account for varying signal amplitudes and noise floors while maintaining an achievable per-implant data rate.  $UL_{DATA}$  is used as the I-DAC code in the uplink modulator. The implants count the Uplink Mode pulses using the US-On block to monitor which implant is in control of the channel. A schematic of the US-On circuitry is shown in Fig. 7(c);  $V^+$  and  $V^-$  are the inverting outputs of the rectifier comparators in Fig. 7(a). When the implant is receiving US power, the NMOS transistors are active and discharge the capacitor, raising the  $US_{ON}$  flag; when the US is off,  $V^+$  and  $V^-$  are pulled down and the capacitor is recharged by the current source. The FSM counts the  $US_{ON}$  signals and uses the uplink index parameter to determine if the implant should transmit data in the current Uplink Mode pulse. If the implant controls the channel, the uplink modulator is activated to perform multi-level ASK backscatter. To evaluate the BER of the communication protocol, a 16-bit LFSR is implemented in the digital backend. If activated during Config Mode, the LFSR block generates a pseudorandom binary sequence (PRBS) that is written to the FIFO memory. To calculate the system BER, the ASK-modulated data sequence received over the US link is compared to the PRBS reference.

### C. Neural Recording AFE

To record neural signals (e.g., LFPs, electromyography (EMG) signals, action potentials, etc.), the DustNet IC implements an analog front-end that consists of a low-noise amplifier and a 12-bit asynchronous SAR ADC. A schematic-level diagram of the neural recording AFE is shown in Fig. 8(a). The low-noise amplifier consists of a chopped  $G_m$  stage ( $f_{chop} = 50$  kHz) followed by a switched-capacitor (SC) integrator. The integrator output is sampled by the SAR ADC at 6.25 kS/s. Depending on the number of ASK levels, a configurable set of 8 or 9 bits from the ADC output are stored in the FIFO buffer to be transmitted back to the external interrogator, yielding a per-implant data rate of 50 or 56.25 kb/s, respectively.

The first  $G_m$  stage consists of a fully-differential OTA, which is used for its high speed and noise efficiency. A common-mode feedback (CMFB) circuit sets the output DC voltage to match a reference supplied by an on-chip LDO. The current from the  $G_m$  cell is integrated on a feedback

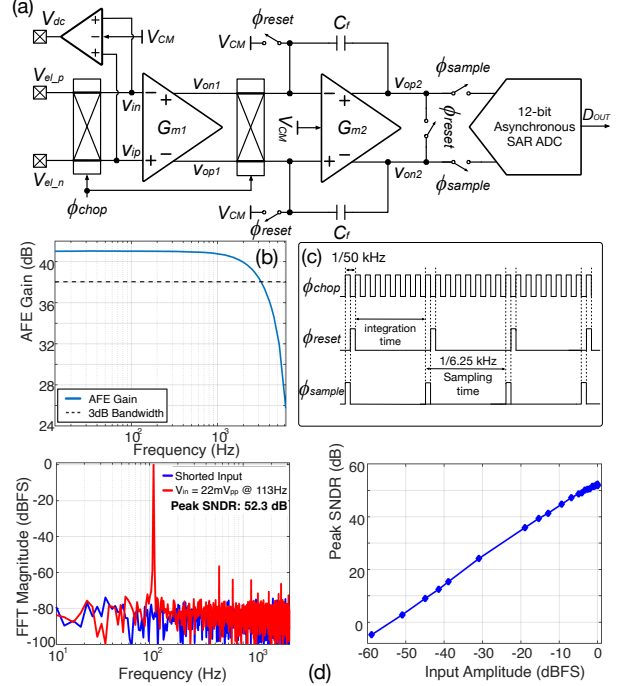


Fig. 8. (a) AFE signal chain consisting of a chopped low-noise  $G_m$ -cell, switched-capacitor integrator, and 12-bit asynchronous SAR ADC. (b) Measured AFE output spectrum and SNDR using a 310Hz input tone. (c) AFE timing diagram. (d) Measured AFE spectrum at maximum SNDR with  $V_{in} = 22mV_{pp}$  and SNDR as a function of input amplitude.

capacitor  $C_f$  in the second stage. The SC integrator consists of a two-stage, Miller-compensated OTA with CMFB. The AFE bandwidth is designed to match the ADC Nyquist frequency, and the overall signal transfer function has nulls at integer multiples of the sampling frequency. By setting  $f_{chop} = 8f_s$ , the AFE cancels both chopping artifacts and upconverted flicker noise and offset-related harmonics. The overall signal DC gain ( $H_0$ ) is designed to be 100 to suppress the ADC quantization noise. Measured AFE gain as a function of frequency is shown in Fig. 8(b). The full-scale range of the ADC is designed to be 2V, yielding a differential input range of approximately 20 mV.

A clock generation circuit provides a stable 50 kHz reference ( $CLK_{LO}$ ) using an offset-compensated RC relaxation oscillator [18]; Monte Carlo simulations demonstrate a global frequency variation of just 0.5% without requiring calibration. An on-chip oscillator is used instead of dividing the extracted US clock to allow the carrier frequency to be tuned to the piezo resonant frequency without altering the data sampling rate.  $CLK_{LO}$  is directly used as  $\phi_{chop}$  to chop the AFE inputs, and is divided by 8 to generate the sampling clock ( $\phi_{sample}$ ) used for ADC or linear feedback shift register (LFSR) sampling. The ADC samples the output of the integrator at 6.25 kHz ( $f_s = f_{chop}/8$ ). A timing diagram of the chop, reset, and sample clocks is shown in Fig. 8(c); the integrator resets one clock cycle ( $\phi_{reset}$ ) after the ADC samples its output.

AFE measurement results are shown in Fig. 8(d) using the 9-bit ADC output backscattered from the chip in the 8-level ASK configuration. With a 113Hz input tone of  $22mV_{pp}$ , the AFE achieves a peak signal-to-noise and distortion ratio (SNDR) of 52.3 dB, yielding an effective number of bits (ENOB) of 8.4

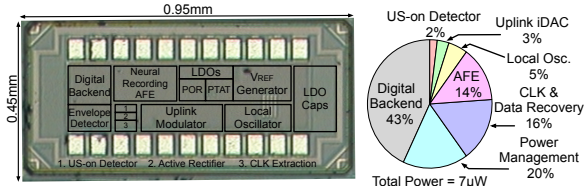


Fig. 9. (a) DustNet IC micrograph highlighting the location of various blocks. The chip occupies a footprint of  $0.43\text{ mm}^2$ . (b) Power breakdown of the IC. The implant consumes a total power of  $7\text{ }\mu\text{W}$ .

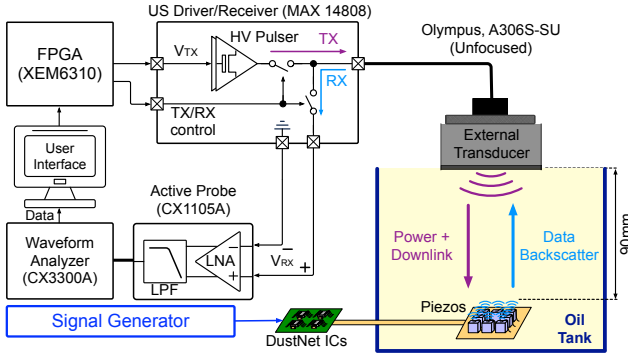


Fig. 10. *In vitro* measurement setup. Implant piezos are mounted on an fPCB submerged 90mm in canola oil and connected via external wires to the DustNet ICs. An FPGA and high voltage US pulser board are used to generate control signals for the external interrogator, and a signal generator supplies pre-recorded neural signals to the ICs.

bits. The dynamic range is measured to be 53.8 dB, which is suitable for neural recording applications. The effective range of the ADC can also be adjusted by configuring the transmitted bits in Config Mode (e.g., ADC MSBs or ADC LSBs). By transmitting the 9 least significant bits of the ADC output, the input-referred integrated noise of the combined amplifier and ADC is measured to be  $9.8\text{ }\mu\text{V}_{\text{rms}}$  across the 3.125 kHz bandwidth.

#### IV. MEASUREMENT RESULTS

The DustNet IC was fabricated in a 28nm CMOS process. A chip micrograph and power breakdown is shown in Fig. 9. The functionality of the DustNet system was verified at 90mm depth in canola oil, which has an acoustic attenuation coefficient ( $\sim 0.25\text{ dB/cm/MHz}$ ) similar to human tissue.

##### A. Measurement Setup & Data Processing

The measurement setup is shown in Fig. 10. Four miniaturized piezoceramic transducers of size  $0.7 \times 0.7 \times 0.7\text{ mm}^3$  with  $f_p \approx 2\text{ MHz}$  are mounted on a flexible PCB (fPCB) using conductive silver epoxy in a tank filled with canola oil. An acoustic absorber (Aptflex F28P, Precision Acoustics) is placed at the bottom of the tank under the fPCB. An unfocused ultrasound transducer (A306S-SU, Evident Scientific) is vertically mounted in the tank 90mm directly above the transducer. Wires connect four DustNet ICs mounted on external daughterboards to the fPCB in the tank.

A 5-level high voltage pulser (MAX14808, Analog Devices) with a built-in TX/RX switch drives the unfocused US transducer at 2 MHz. An FPGA (XEM6310, OpalKelly)

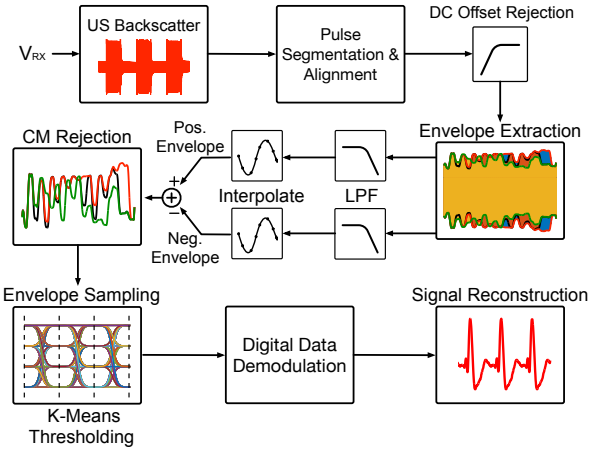


Fig. 11. Signal processing chain to demodulate data encoded in the US backscatter.  $V_{\text{RX}}$  is recorded directly from the output of the HV pulser board. After demodulation of the individual pulses, data are concatenated to reconstruct the recorded ADC/LFSR output.

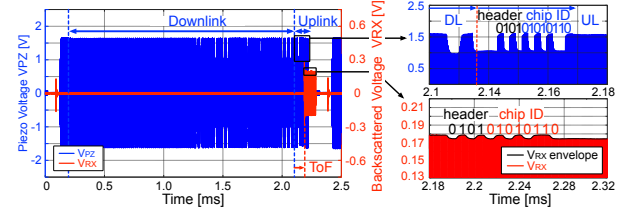


Fig. 12. Measured Config Mode waveform at the implant piezo (blue) and implant backscatter received at the external interrogator (red). Because the target ID matches the implant ID, the implant backscatters its own ID, which arrives at the external interrogator after 1 ToF.

generates control signals for the pulser to form the Config Mode and Uplink Mode packets. To record the US backscatter, the pulser switches to RX mode one ToF after the chip begins to transmit data. The received voltage ( $V_{\text{RX}}$ ) is recorded by a low-noise active probe (CX1105A, Keysight) with a 10 MHz low-pass filter (LPF) connected to a high-resolution current waveform analyzer (CX3300A, Keysight).

To decode ASK-modulated data from the received backscatter waveforms, several signal processing techniques are used to extract the US envelope and remove out-of-band noise and other undesired fluctuations. A complete block diagram of all the signal processing steps used to demodulate the US backscatter is shown in Fig. 11. First, the timeseries Uplink Mode waveform obtained from the current waveform analyzer is segmented into individual pulses that are time-aligned based on the start of the US pulse. The segments are high-pass filtered using a Butterworth filter with a high pass corner at 20 kHz to remove DC offsets and low-frequency noise. The US envelope is extracted from the peaks and valleys of the recorded US backscatter using spline interpolation. The envelope is then low-pass filtered using a second-order Type 2 Chebyshev filter with a low-pass corner at 10 MHz to eliminate high-frequency noise. Common-mode noise is eliminated by taking the difference between the positive and negative envelope waveforms.

The envelope waveforms are sampled at the end of each transmitted symbol and thresholds for each amplitude level

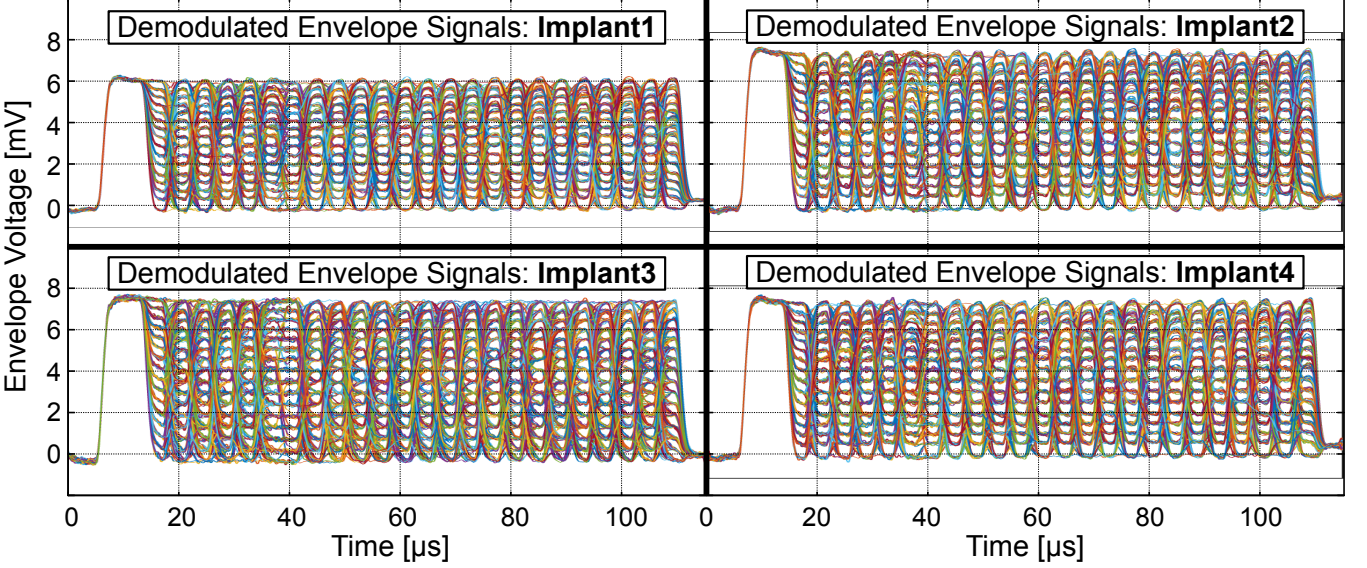


Fig. 13. (a) Backscattered Uplink Mode waveforms received at the external interrogator (red) when the system is configured to support 8 implants with 4 implants enabled, and the piezo voltage of implant 1 (blue) demonstrating the TDMA protocol. (b) Demodulated eye diagrams for four implants transmitting data using 16-level ASK modulation over the ultrasound link. The received echo levels are clearly separable, indicating that no errors were made.

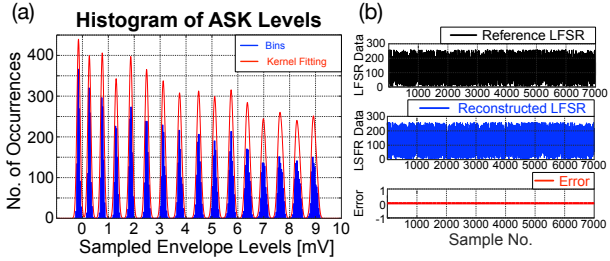


Fig. 14. (a) A histogram of envelope voltages extracted from 827 Uplink Mode packets modulated with LFSR data with a fitted PDF demonstrating 16 separable levels. (b) Reconstructed LFSR data (blue) compared to a golden reference (black). No errors (red) are made when transmitting 52928 bits, yielding a BER of  $\leq 1.89E-5$ .

are generated using k-means clustering of the received echo voltages. To demodulate the data, these thresholds are used to convert each symbol into a 4-bit binary representation, and pairs of transmitted symbols are combined to recover the 8-bit data samples. The system BER is characterized by transmitting PRBS data generated by the on-chip LFSR and comparing the received bitstream to a golden reference.

#### B. Communication Protocol Verification & Implant Measurements

When the US pulser is initially turned on, the DustNet ICs begin to charge their  $C_{store}$ .  $V_{RECT}$  settles to a value  $>1.2V$ ; the achieved voltage varies depending on the US power transmitted by the external interrogator. The regulated supplies  $V_{DD,A}$  and  $V_{DD,D}$  settle to 1.0V and 0.8V, respectively. Once the LDO voltages have settled, the  $V_{POR}$  flag is raised to activate the digital backend.

An example Config Mode waveform ( $V_{PZ}$ ) and the corresponding backscatter received at the external interrogator ( $V_{RX}$ ) are shown in Fig. 12.  $V_{PZ}$  is recorded at the piezo terminals, and the modulated uplink section is received as

$V_{RX}$  after 1 ToF. The header and chip ID backscattered by the uplink modulator are clearly seen in both  $V_{PZ}$  and  $V_{RX}$ . Because the carrier frequency is equal to  $f_p$ , a high  $V_{PZ}$  results in a low  $\Gamma_p$  and thus a low  $V_{RX}$ .

To validate the multi-implant TDMA protocol, each implant transmits PRBS data from its on-chip LFSR. A sample set of backscattered Uplink Mode waveforms are shown in Fig. 13(a), in which the system is configured to support 8 total implants with data transmission enabled for 4 implants. Amplitude modulation for each transmitting implant is clearly demonstrated in the recorded backscatter. The recorded  $V_{PZ}$  for implant 1 is also shown in Fig. 13(a). Because  $N_{implants} = 8$  is set in Config Mode, each implant backscatters its data once out of every 8 pulses. Eye diagrams for the 16-level ASK backscatter received from each implant using are shown in Fig. 13(b). The ASK levels are clearly separable, indicating that no errors are made during transmission. The peak envelope voltage received from each implant varies slightly due to mismatch across the implant ICs and piezos. However, unlike for CDMA protocols, this does not pose an issue to decoding because packets received from different piezos are processed separately, and a set of ASK thresholds are generated for each chip. Each implant transmits 24 4-bit symbols (96 total bits) during each set of 8 US pulses (duration: 1.9ms). This corresponds to a per-implant data rate of 50kb/s; with the system capable of supporting 8 total implants, these measurements demonstrate a total system data rate of 400 kb/s.

A histogram of received backscatter voltages from 827 Uplink Mode packets transmitted by a single implant and a fitted probability distribution (PDF) is shown in Fig. 14(a). The voltage levels are clearly separable and the PDF shows 16 distinct peaks. A plot of the reconstructed data and golden reference data is shown in Fig. 14(b); there are no errors in the transmitted data stream. The data stream consists of 6616 8-bit samples, yielding a BER of  $\leq 1.89E-5$ .

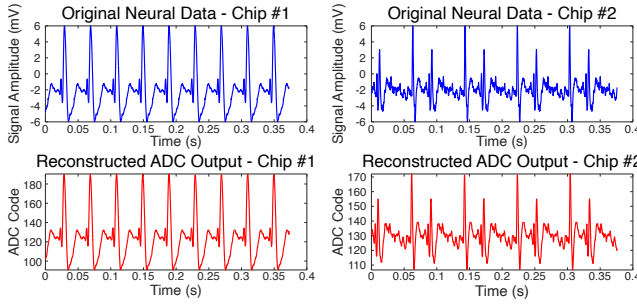


Fig. 15. End-to-end system verification. Simulated neural signals (blue) are fed to the implant using a function generator and off-chip electrode model. The signals are quantized by the on-chip AFE and the digital data is transmitted over the US link. Demodulated data (red) closely matches the original neural data.

TABLE II  
COMPARISON OF WIRELESS NEURAL IMPLANT SYSTEMS

	This work	[7]	[4]	[5]	[6]
Wireless Link	<b>US</b>	US	RF	RF / NIR	ME / Inductive
Max Depth [mm]	<b>90</b>	50	5	2	60
Data Uplink Protocol	<b>ASK16</b>	Analog AM	BPSK	LSK (RF)	LSK (Inductive)
Downlink Protocol	<b>ASK2</b>	N/A	ASK-PWM	PWM (Optical)	TDM (ME)
Multiple Access Protocol	<b>TDMA</b>	CDMA	TDMA	CDMA	FDMA
Max # of Implants	<b>8</b>	2	770	N/A	15
Measured # of Implants	<b>4</b>	2	48	4	15 (DL) / 1 (UL)
Carrier Frequency [MHz]	<b>2</b>	1.78	915	3000	0.31 (DL) / 31 (UL)
Total Data Rate (kb/s)	<b>400</b>	70	10000	0.000312	40
Process [nm]	<b>28</b>	65	65	180	180
IC Area [mm <sup>2</sup> ]	<b>0.43</b>	0.25	0.42	0.07	0.99
IC Power [μW]	<b>7</b>	38	30	0.57	11
Spectral Efficiency <sup>1</sup> [kb/s/MHz]	<b>200</b>	39	11	0.0001	1.3
BER	<b>1.9E-5 @ 90mm</b>	N/A	5E-3 @ 5mm	1E-6 @ 2mm	5.5E-5 @ 20mm

<sup>1</sup>Total data rate / carrier frequency

To demonstrate end-to-end functionality, the AFE inputs of two implants are connected to an arbitrary function generator programmed to output simulated, slowed neural waveforms. The 8 MSBs of the on-chip ADC outputs are then transmitted over the US link. Fig. 15 shows the time-aligned simulated neural waveforms and reconstructed ADC outputs for both implants; the ADC sampling rate is approximately 6.25 kHz for both implants, yielding a data rate of 50 kb/s for each implant.

## V. SUMMARY AND COMPARISON

A comparison to prior wireless, chip-based multi-implant systems is shown in Table II. The proposed system uses a

16-level ASK modulation scheme to transmit neural data over an ultrasound link, enabling a total data rate of 400 kb/s at a carrier frequency of 2 MHz. Using a TDMA protocol to communicate with multiple implants, the proposed system also demonstrates the highest number of simultaneously-recording US-powered implants to date. DustNet can operate at depths in excess of 90mm, which is 15x deeper than comparable RF- or NIR-powered neural implants. Furthermore, the 16-level ASK modulation scheme enables highly efficient use of the channel bandwidth; this results in DustNet's highest spectral efficiency of 200 kb/s/MHz, which is 5x higher than other state-of-the-art multi-implant systems. Because the system data rate scales linearly with the US carrier frequency, the number of implants can be increased by increasing the transmitted US frequency until inter-symbol interference degrades the system BER. Increasing the data rate by raising the US carrier frequency would also enable further miniaturization by reducing the implant piezo volume.

## ACKNOWLEDGMENTS

The authors thank the National Science Foundation Graduate Research Fellowship, the Weill Neurohub Fellowship, and the sponsors of the Berkeley Wireless Research Center. The authors also thank TSMC for sponsoring chip fabrication.

## REFERENCES

- [1] B. Lee, M. K. Koripalli, Y. Jia, J. Acosta, M. S. E. Sendi, Y. Choi, and M. Ghovalloo, "An Implantable Peripheral Nerve Recording and Stimulation System for Experiments on Freely Moving Animal Subjects," *Scientific Reports*, vol. 8, no. 1720, p. 6115, Apr. 2018, publisher: Nature Publishing Group.
- [2] P. P. Vu, A. K. Vaskov, Z. T. Irwin, P. T. Henning, D. R. Lueders, A. T. Laidlaw, A. J. Davis, C. S. Nu, D. H. Gates, R. B. Gillespie, S. W. P. Kemp, T. A. Kung, C. A. Chestek, and P. S. Cederna, "A regenerative peripheral nerve interface allows real-time control of an artificial hand in upper limb amputees," *Science translational medicine*, vol. 12, no. 533, p. eaay2857, 2020.
- [3] P. Čvančara, G. Valle, M. Müller, I. Bartels, T. Guiho, A. Hiairassary, F. Petrini, S. Raspopovic, I. Strauss, G. Granata, E. Fernandez, P. M. Rossini, M. Barbaro, K. Yoshida, W. Jensen, J.-L. Divoux, D. Guiraud, S. Micera, and T. Steiglitz, "Bringing sensation to prosthetic hands—chronic assessment of implanted thin-film electrodes in humans," *Npj Flexible Electronics*, vol. 7, no. 1, p. 51, 2023.
- [4] J. Lee, V. Leung, A.-H. Lee, J. Huang, P. Asbeck, P. P. Mercier, S. Shellhammer, L. Larson, F. Laiwalla, and A. Nurmikko, "Neural recording and stimulation using wireless networks of microimplants," *Nature Electronics*, vol. 4, no. 8, pp. 604–614, 2021.
- [5] G. Atzeni, J. Lim, J. Liao, A. Novello, J. Lee, E. Moon, M. Barrow, J. Letner, J. Costello, S. R. Nason, P. R. Patel, P. G. Patil, H.-S. Kim, C. A. Chestek, J. Phillips, D. Blaauw, and T. Jang, "A 260×274 μm<sup>2</sup> 572 nw neural recording micromote using near-infrared power transfer and an rf data uplink," in *2022 IEEE Symposium on VLSI Technology and Circuits (VLSI Technology and Circuits)*, 2022, pp. 64–65.
- [6] Z. Yu, W. Wang, J. C. Chen, Z. Chen, Y. He, A. Singer, J. T. Robinson, and K. Yang, "A wireless network of 8.8-mm<sup>3</sup> bio-implants featuring adaptive magnetoelectric power and multi-access bidirectional telemetry," in *2022 IEEE Radio Frequency Integrated Circuits Symposium (RFIC)*, 2022, pp. 47–50.
- [7] M. M. Ghanbari, D. K. Piech, K. Shen, S. Faraji Alamouti, C. Yalcin, B. C. Johnson, J. M. Carmena, M. M. Maharbiz, and R. Muller, "A sub-mm<sup>3</sup> ultrasonic free-floating implant for multi-mote neural recording," *IEEE J. Solid-State Circuits*, vol. 54, no. 11, pp. 3017–3030, 2019.

- [8] S. F. Alamouti, M. M. Ghanbari, N. T. Ersimo, and R. Muller, "High throughput ultrasonic multi-implant readout using a machine-learning assisted CDMA receiver," in *2020 42nd Annual International Conference of the IEEE Engineering in Medicine & Biology Society (EMBC)*, pp. 3289–3292, ISSN: 2694-0604.
- [9] M. M. Ghanbari and R. Muller, "Optimizing volumetric efficiency and backscatter communication in biosensing ultrasonic implants," *IEEE Transactions on Biomedical Circuits and Systems*, vol. 14, no. 6, pp. 1381–1392, 2020.
- [10] H. G. Rey, C. Pedreira, and R. Q. Quiroga, "Past, present and future of spike sorting techniques," *Brain research bulletin*, vol. 119, pp. 106–117, 2015.
- [11] C. Lee, J. Pinkenburg, M. M. Ghanbari, C. Yalcin, M. Montalban, and R. Muller, "35.8 dustnet: A network of time-division multiplexed ultrasonic implants with 16-level ask backscatter modulation," in *2025 IEEE International Solid-State Circuits Conference (ISSCC)*, vol. 68, 2025, pp. 582–584.
- [12] T. C. Chang, M. L. Wang, J. Charthad, M. J. Weber, and A. Arbabian, "27.7 a 30.5 mm 3 fully packaged implantable device with duplex ultrasonic data and power links achieving 95kb/s with 10- 4 ber at 8.5 cm depth," in *2017 IEEE International Solid-State Circuits Conference (ISSCC)*. IEEE, 2017, pp. 460–461.
- [13] D. Seo, R. M. Neely, K. Shen, U. Singhal, E. Alon, J. M. Rabaey, J. M. Carmena, and M. M. Maharbiz, "Wireless recording in the peripheral nervous system with ultrasonic neural dust," *Neuron*, vol. 91, no. 3, pp. 529–539, 2016.
- [14] T. C. Chang, M. Wang, and A. Arbabian, "Multi-access networking with wireless ultrasound-powered implants," in *2019 IEEE Biomedical Circuits and Systems Conference (BioCAS)*. IEEE, 2019, pp. 1–4.
- [15] B. A. Ozilgen and M. M. Maharbiz, "Ultrasonic thermal dust: A method to monitor deep tissue temperature profiles," in *2017 39th Annual International Conference of the IEEE Engineering in Medicine and Biology Society (EMBC)*. IEEE, 2017, pp. 865–868.
- [16] M. Roschelle, R. Rabbani, S. Gweon, R. Kumar, A. Vercruyse, N. Woo Cho, M. H. Spitzer, A. M. Niknejad, V. M. Stojanović, and M. Anwar, "A wireless, multicolor fluorescence image sensor implant for real-time monitoring in cancer therapy," *IEEE Journal of Solid-State Circuits*, vol. 59, no. 11, pp. 3580–3598, 2024.
- [17] S. Sonmezoglu and M. M. Maharbiz, "34.4 a 4.5 mm 3 deep-tissue ultrasonic implantable luminescence oxygen sensor," in *2020 IEEE International Solid-State Circuits Conference-(ISSCC)*. IEEE, 2020, pp. 454–456.
- [18] A. Paidimarri, D. Griffith, A. Wang, G. Burra, and A. P. Chandrakasan, "An rc oscillator with comparator offset cancellation," *IEEE Journal of Solid-State Circuits*, vol. 51, no. 8, pp. 1866–1877, 2016.